NANO LETTERS

Letter

pubs.acs.org/NanoLett

Surface Plasmon Polariton Graphene Photodetectors

T.J. Echtermeyer,[†,‡] S. Milana,[†] U. Sassi,[†] A. Eiden,[†] M. Wu,[†] E. Lidorikis,[§] and A.C. Ferrari*[,†]

[†]Cambridge Graphene Centre, University of Cambridge, Cambridge CB3 0FA, United Kingdom

[‡]School of Electrical & Electronic Engineering, University of Manchester, Manchester M13 9PL, United Kingdom

[§]Department of Materials Science & Engineering, University of Ioannina, Ioannina 45110, Greece

ABSTRACT: The combination of plasmonic nanoparticles and graphene enhances the responsivity and spectral selectivity of graphene-based photodetectors. However, the small area of the metal−graphene junction, where the induced electron−hole pairs separate, limits the photoactive region to submicron length scales. Here, we couple graphene with a plasmonic grating and exploit the resulting surface plasmon polaritons to deliver the collected photons to the junction region of a metal−graphene−metal photodetector. This gives a 400% enhancement of responsivity and a 1000% increase in photoactive length, combined with tunable spectral selectivity. The interference between surface plasmon polaritons and the incident wave introduces new functionalities, such as light flux attraction or repulsion from the contact edges, enabling the tailored design of the photodetector's spectral response. This architecture can also be used for surface plasmon biosensing with direct-electric-redout, eliminating the need of bulky optics.

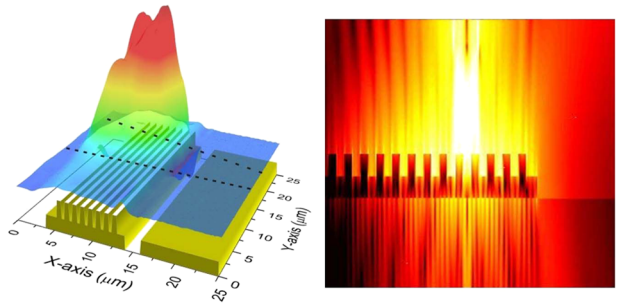

KEYWORDS: *graphene, photodetection, plasmonics, surface plasmon polariton, sensor*

Graphene-based photodetectors (PDs)[1,2] have been reported with ultrafast operating speeds (up to 262 GHz from the measured intrinsic response time of graphene carriers[3]) and broadband operation from the visible and infrared[3−16] up to the THz.[17−19] The simplest graphene-based photodetection scheme relies on the metal−graphene-metal (MGM) architecture,[5,7,8,11,20−22] where the photoresponse is due to a combination of photothermoelectric and photovoltaic effects.[5,7,8,11,20−22] For both mechanisms, the presence of a junction is required to spatially separate excited electron−hole (e−h) pairs.[5,7,8,11,20−22] At the metal−graphene junction, a work-function difference causes charge transfer and a shift of the graphene Fermi level underneath the contact,[4,5,7,23] compared to that of graphene away from the contact,[4,5,7,23] resulting into a buildup of an internal electric field (photovoltaic mechanism)[5,7,24,25] and into a difference of Seebeck coefficients (photothermoelectric mechanism).[11,21,26] An alternative way to create a junction is to use a set of gate electrodes to electrostatically dope graphene.[8,11]

For both photovoltaic and photothermoelectric mechanisms, however, the spatial extend of the junction is ∼100−200 nm,[7,8,11] which reduces the photoactive area to a fraction of the diffraction limited laser spot size in a typical scanning current microscopy experiment. Furthermore, suspended undoped graphene only absorbs 2.3% of light[27] which, though remarkably high for a one atom thick material, is low in absolute terms for practical applications. This is further reduced by a factor $4/(1 + n)^2$ for graphene on a dielectric substrate of refractive index n [see Methods]. Additionally, in highly doped graphene the absorption decreases even further.[28,29]

One approach is to extend the junction region in order to capture more light. In a vertical (i.e., with doping profile perpendicular to the device's surface) p−i−n semiconductor PD, this is achieved by ion-implantation with tailored dose and energy.[30] In the MGM configuration, however, the lateral nature of the junction (i.e., doping profile parallel to the device's surface) does not allow a straightforward doping profile engineering and, thus far, to the best of our knowledge, no techniques have been reported to reliably do that. As an alternative, several graphene-based vertical architectures have been proposed, including all-graphene,[31] or graphene integrated with semiconductor layers, such as other two-dimensional (2d) materials[32,33] or Si.[34,35] In the latter cases, however, graphene is not the absorbing material and the spectral response is thus limited to above the band gap of the semiconductor layer. Furthermore, although these approaches have demonstrated high responsivities (up to∼ 5×10^8A/W in ref 33 by employing MoS_2 as light capturing material), they do come at the cost of smaller operation speed (up to a maximum of 100 kHz in ref 31) as compared to the graphene-based PDs operating at speeds up to 50 GBit/s in the optical link reported in ref 36.

Improving graphene absorption in the ultrafast MGM configuration is thus critical. Various solutions have been proposed, such as the integration of graphene into an optical

Received: May 25, 2015
Revised: November 12, 2015
Published: December 14, 2015

DOI: 10.1021/acs.nanolett.5b02051
Nano Lett. 2016, 16, 8−20

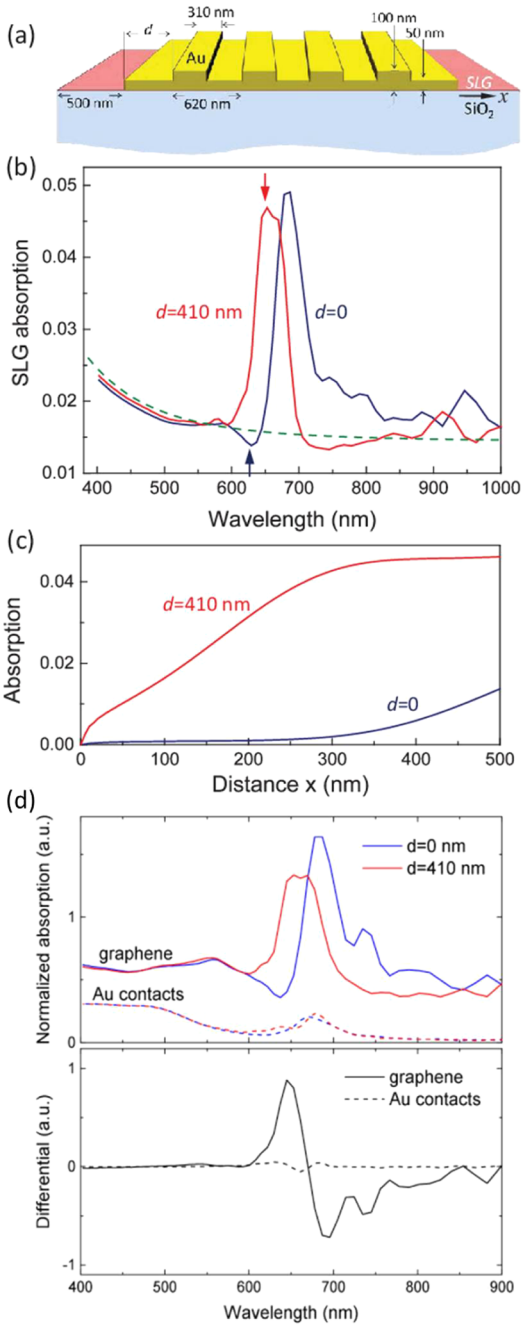

Figure 1. (a) Schematic of the simulated structure. (b) Relative (i.e., normalized to the case without the grating) absorption in the exposed SLG. (c) Cumulative absorption in the exposed SLG integrated away from the contact edge, for the two cases pointed by the arrows in (b). (d) Absorption in graphene and Au contacts normalized to their thickness and volumetric heat capacity and differential absorption in graphene and the Au contacts.

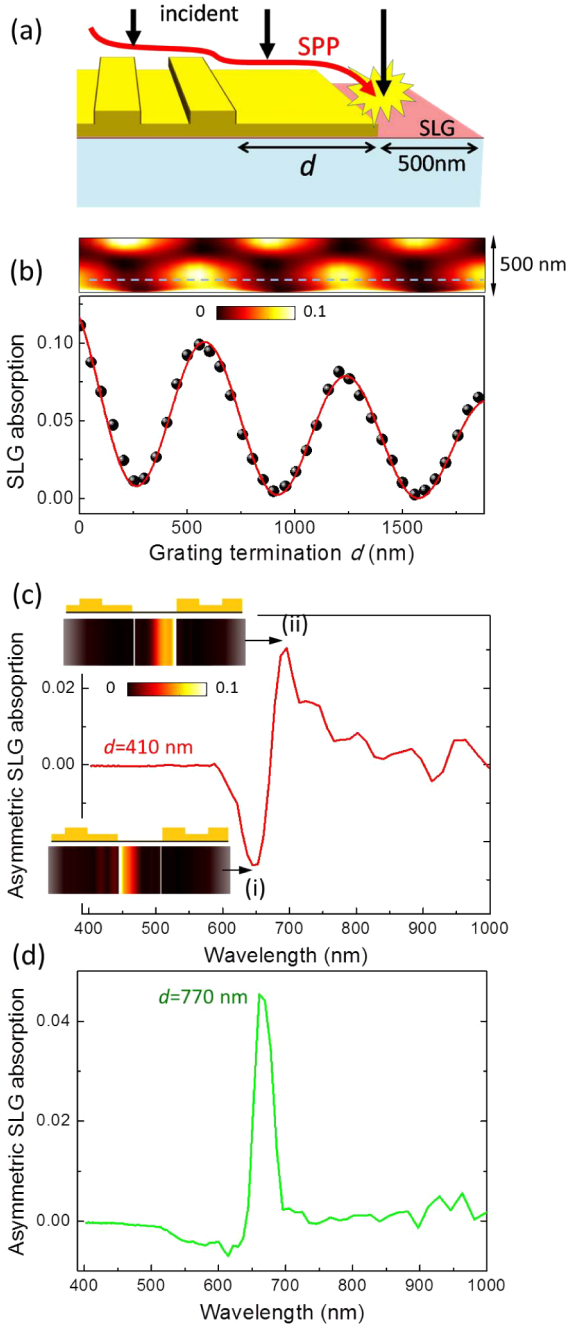

Figure 2. (a) Depiction of the interference mechanism. (b) Relative (i.e., normalized to the case without the grating) SLG absorption within 100 nm from the contact edge as a function of d. The line is a fit of eq 4, which assumes SPP + incident wave interference. The top inset color-codes the absorption distribution in the exposed SLG as a function of d. (c) Asymmetric contact layout with d = 0 and 410 nm, as shown in the insets, with 600 nm exposed SLG width. The asymmetric absorption (i.e., $A_R - A_L$, where A_R and A_L are the SLG absorptions in the right and left halves of the SLG channel) is proportional to the net photovoltage under coherent uniform illumination. The insets color-code the absorption profiles for the two peaks indicated by the arrows. (d) Asymmetric absorption when the 410 nm contact is replaced by a 770 nm one.

microcavity[37,38] (>20-fold enhancement) or onto a planar photonic crystal cavity[39] (8-fold enhancement), to take advantage of the multiple passes of the trapped light through graphene, or its coplanar integration with a Si integrated photonic waveguide[40−42] (>10-fold enhancement). Another option is the integration of plasmonic nanostructures on graphene[9,10,43] to exploit the strongly enhanced electromagnetic near-fields[44,45] associated with localized surface plasmon resonances (LSPRs).[44,45] LSPRs originate from the resonant coherent oscillation of a metal's conduction electrons in response to incident radiation. The resulting enhanced near-fields surrounding the nanostructures promote light absorption in the materials around them.[44] We previously reported a ×20

DOI: 10.1021/acs.nanolett.5b02051
Nano Lett. 2016, 16, 8−20

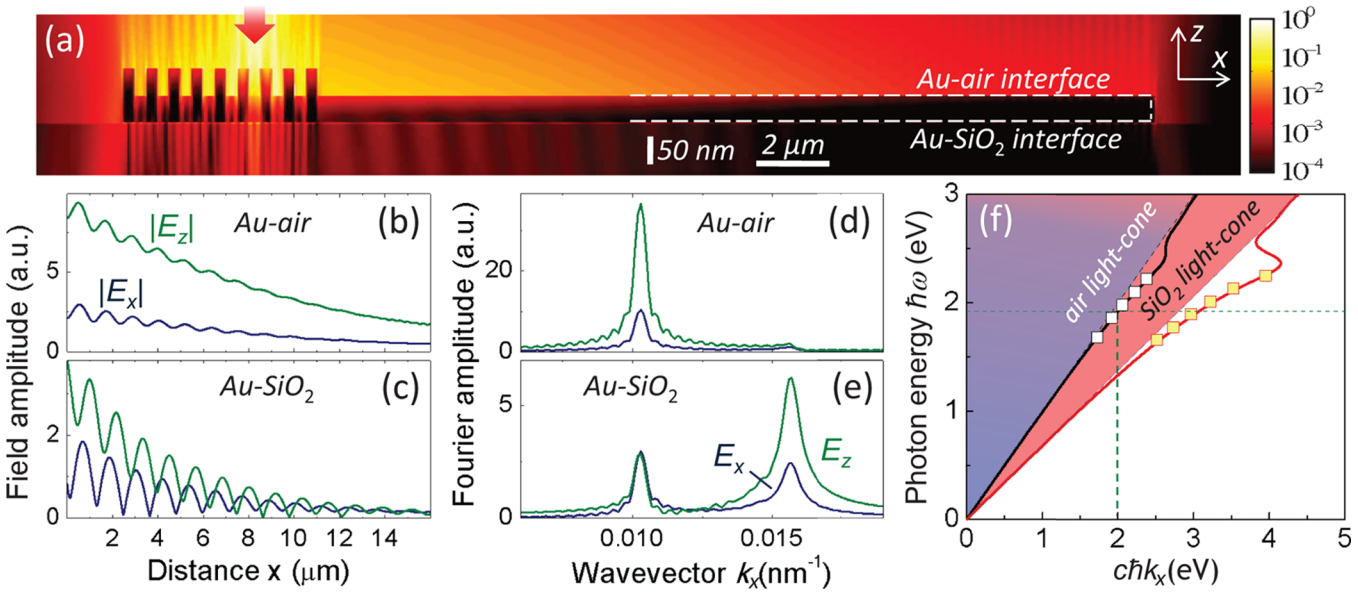

Figure 3. (a) Field intensity distribution for 650 nm focused illumination (1 μm spot size) of a contact with a large d = 20 μm on one side. (b,c) Field amplitude profiles along the Au−air and Au−SiO_2 interfaces. (d,e) Spatial Fourier amplitudes of the fields along the interfaces. (f) Dispersion relations between frequency and real part of the wavevector. The lines are from eq 1 and the squares are the peaks of the simulated Fourier amplitudes. The vertical and horizontal dashed lines denote the SPP condition in eq 1 with a = 620 nm. The light lines of the two dielectric media (air and SiO_2) extend between the vertical axis at k_x = 0 (normal incidence) to the $k_x = n\omega/c$ line (90° incidence), defining the phase-space of allowed free-propagation modes in the index n medium.

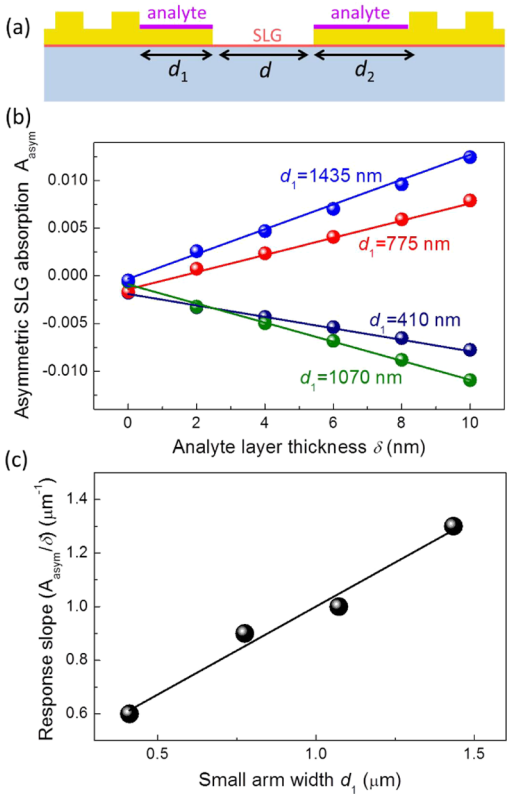

Figure 4. (a) Schematic biosensing device. d = 600 nm is assumed for the exposed SLG. An analyte (purple) is deposited on both sensor arms. (b) Asymmetric absorption (proportional to the net photovoltage) as a function of analyte thickness for four sensor arm pairs. The operating wavelength is 678 nm. (c) Response curve slope as a function of small sensor arm length.

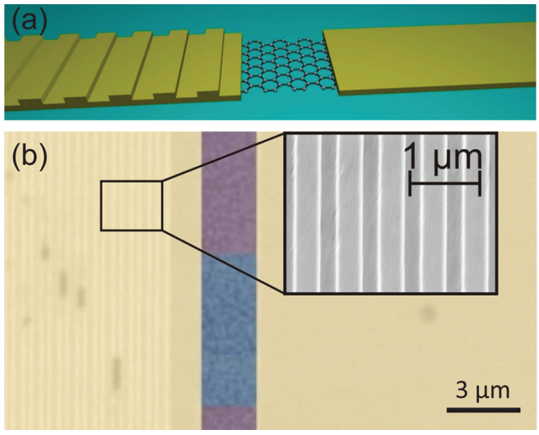

Figure 5. MGM-PD with plasmonic grating coupler. (a) Schematic and (b) SEM micrograph.

enhancement in photoresponse[9] for radiation focused close to the nanostructures. In that approach, however, light absorbed around nanostructures far from the junction (where efficient charge separation occurs) does not fully contribute to the photoresponse.[43]

An ideal alternative would be to enable light collection in one part of a device and then guide it into the junction region at the contact edge. This can be achieved by exciting surface plasmon polaritons (SPPs) on the metal contacts. SPPs are surface-bound waves propagating on a metal-dielectric interface and originate from the coupling of light with the metal's free electrons.[45−47] Their excitation can be achieved by means of an integrated diffraction grating,[45,46] and their delivery to the active region (junction at contact edge) will enhance the overall absorption. Thus, the contact now becomes a light collector. Such an approach was demonstrated with semiconductor-based near-infrared (NIR) PDs[48−53] in order to reduce the

DOI: 10.1021/acs.nanolett.5b02051
Nano Lett. 2016, 16, 8−20

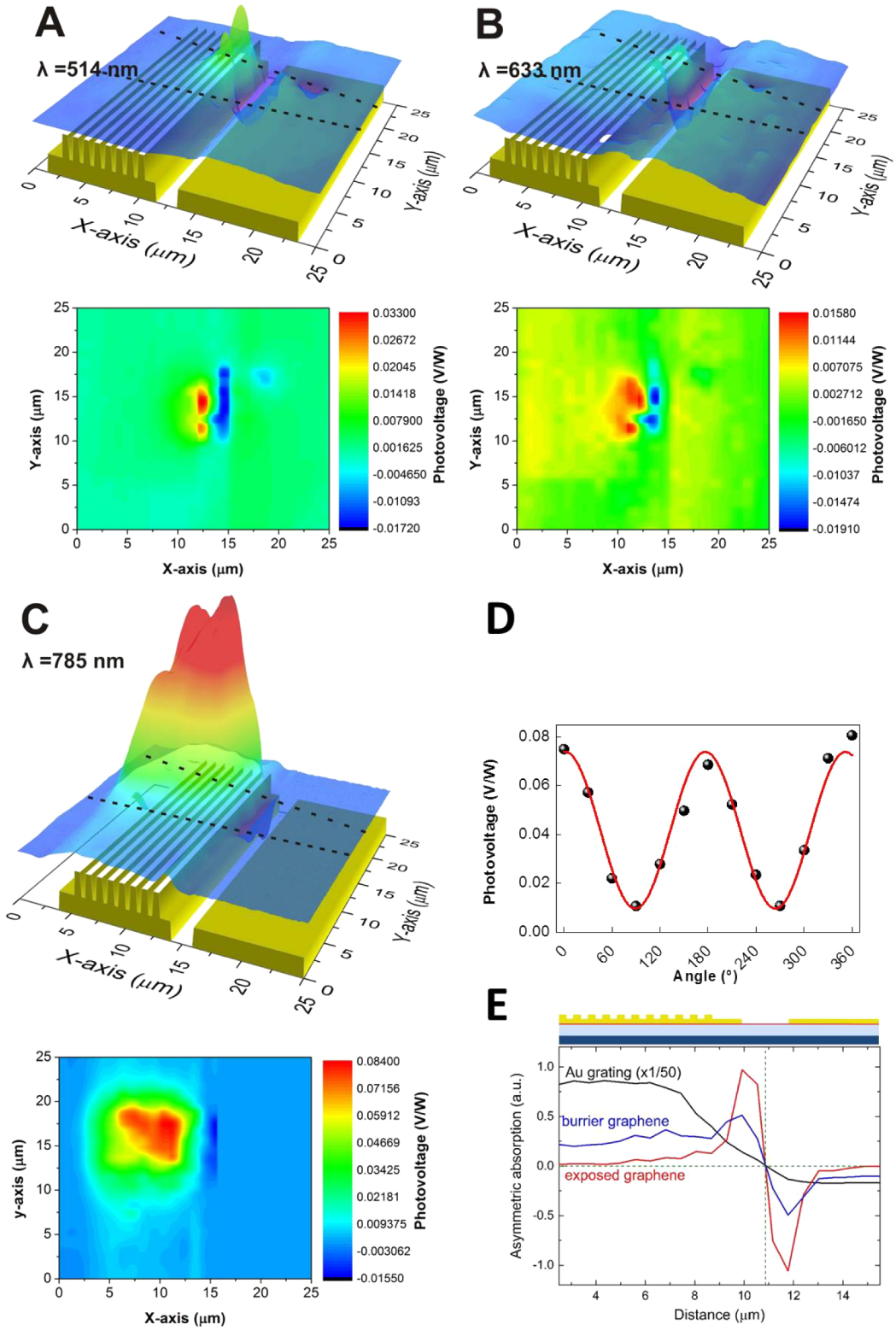

Figure 6. Scanning photovoltage maps for excitations at (a) 514 nm, (b) 633 nm, (c) 785 nm and perpendicular polarization (TM). The grating coupler dimensions are not to scale in the vertical direction. (d) Photovoltage at 785 nm as a function of polarization. 0° denotes TM polarization. (e) Simulation of asymmetric absorption as a function of distance from the contact, the buried and exposed graphene, respectively.

semiconductor active area without compromising light absorption. A smaller active area also decreases the carrier transit time[48,49] and capacitance,[48,49] thus increasing operation speed. In particular, a circular (bull's eye) grating[48,49] was used to deliver SPPs into a subwavelength circular aperture on top of a vertical Si[48] or Ge[49] Schottky photodiodes, while a linear grating was used to deliver SPPs into a subwavelength linear slit in a lateral metal−GaAs−metal photodiode configuration.[52,53] Operation speeds beyond 100 GHz were estimated,[48,49] whereas responsivity enhancements (compared to a device

DOI: 10.1021/acs.nanolett.5b02051
Nano Lett. 2016, 16, 8−20

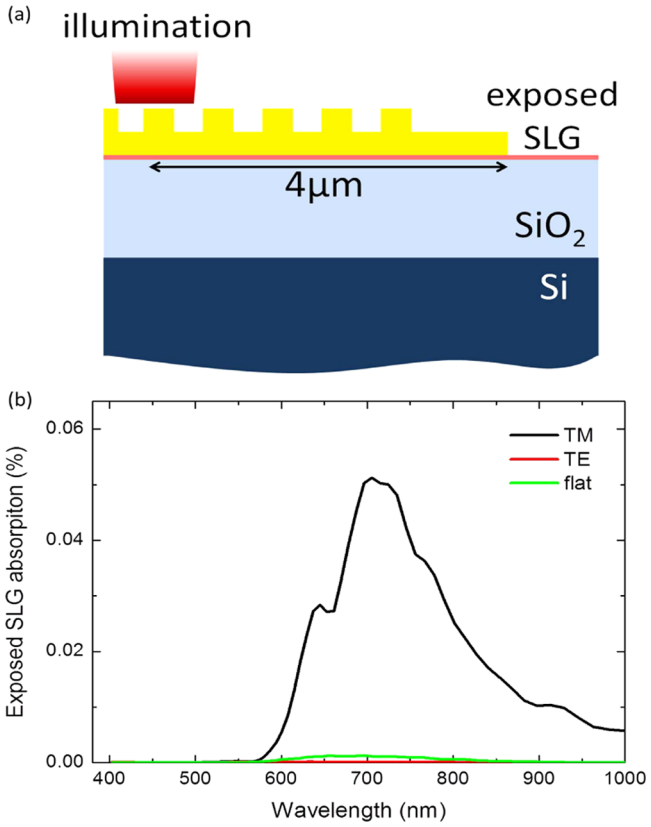

Figure 7. Calculated absorption in the SLG exposed part when a 1 μm spot size illuminates the grating 4 μm away from the metal/SLG junction. (a) Schematic of the simulation system. A thickness of 300 nm SiO_2 on Si is assumed, as for experiments. (b) Absorption in SLG. Two polarizations and a flat contact case are considered.

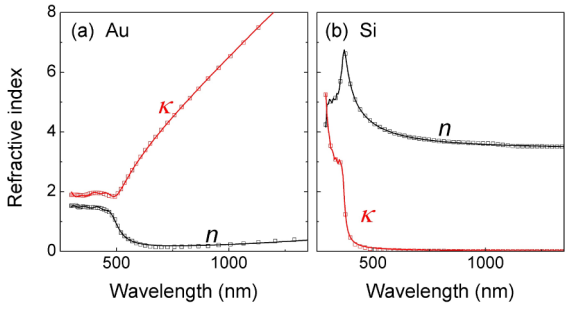

Figure 8. Refractive indexes used in the calculations for (a) Au and (b) Si. Symbols are experimental data from refs 64 and 66; lines are the corresponding Drude–Lorentz fits.

without the grating) were up to ×4 for linear gratings[52,53] and over ×10 for circular gratings.[48,49] No compromise in operation speed was reported due to the presence of the grating.[52] Thus, integration of a grating in a graphene-based PD potentially allows the independent optimization of the light capturing area, which is determined by the grating, and the operating speed of the device, which is determined by the carrier transit time between the contacts.[48,49] This will allow to further exploit graphene in ultrafast PDs.[54,55] A grating was also applied in mid-IR detection,[56] by delivering light into a quantum cascade detector, and in THz detection,[57] by delivering light into a GaAs/AlGaAs 2d-electron–gas bolometer. As such, the contact played an active role for light absorption, instead of being just a passive element, off which most of the light is reflected.[5−7] It

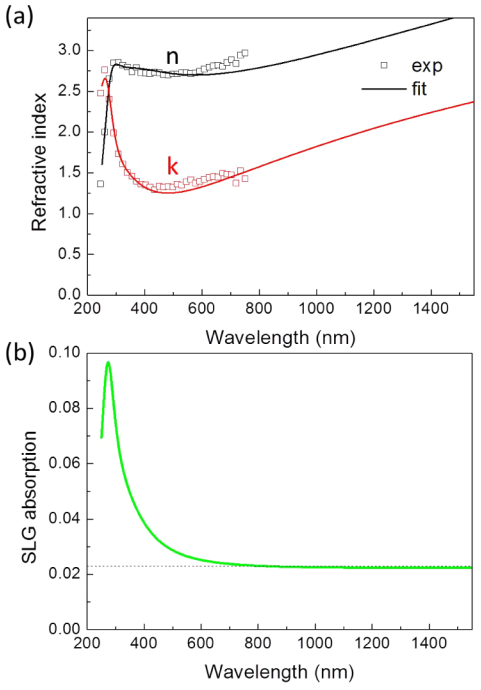

Figure 9. (a) SLG refractive index used in our calculations. Symbols are ellipsometric data from ref 65. (b) SLG absorption corresponding to the refractive index in (a).

delivers light energy that is otherwise lost to the metal–graphene junction. In devices with an unpatterned contact, the photoactive region is determined only by the junction formed in graphene at the contact edge.[5−7] Graphene further away from this edge does not contribute to the photoresponse, as no band bending, thus no potential gradient, is present to separate the excited electron–hole pairs.[5−7] This design enables the increase of the photoactive area by utilizing the normally passive contacts as light collecting elements.

Here, we apply the SPP grating coupler concept to a MGM PD and demonstrate a ∼400% increase in responsivity and a ∼1000% increase in photoactive length. Furthermore, we show that this offers a solution to another problem: in order to have a net response under uniform illumination of the whole MGM PD area, one must break the mirror symmetry between the two contacts.[6] In contrast to the metal–semiconductor–metal case, applying a bias is not practical, because it would result into a large dark current, due to the semimetallic nature of graphene.[6] Using different metallizations for the two contacts is an option,[6] but increases the fabrication steps. In our approach, this problem is addressed by using different contact grating structures. One can utilize the interference between SPPs and incident waves and create novel asymmetric contact designs that produce complex spectral responses, such as switching the light flux between the two contacts edges, enabling new functionalities, including label- and optics-free direct-electrical-readout plasmonic biosensing.

To explore the opportunities offered by a SPP grating coupler on the metal contacts, we first carry out numerical simulations using the finite-difference time-domain (FDTD) method.[44,58] The SPP wavevector on a metal–dielectric interface is[45]

$$k_{SPP} = (\omega/c)\sqrt{(\epsilon_m\epsilon_d)/(\epsilon_m + \epsilon_d)} \quad (1)$$

DOI: 10.1021/acs.nanolett.5b02051
Nano Lett. 2016, 16, 8−20

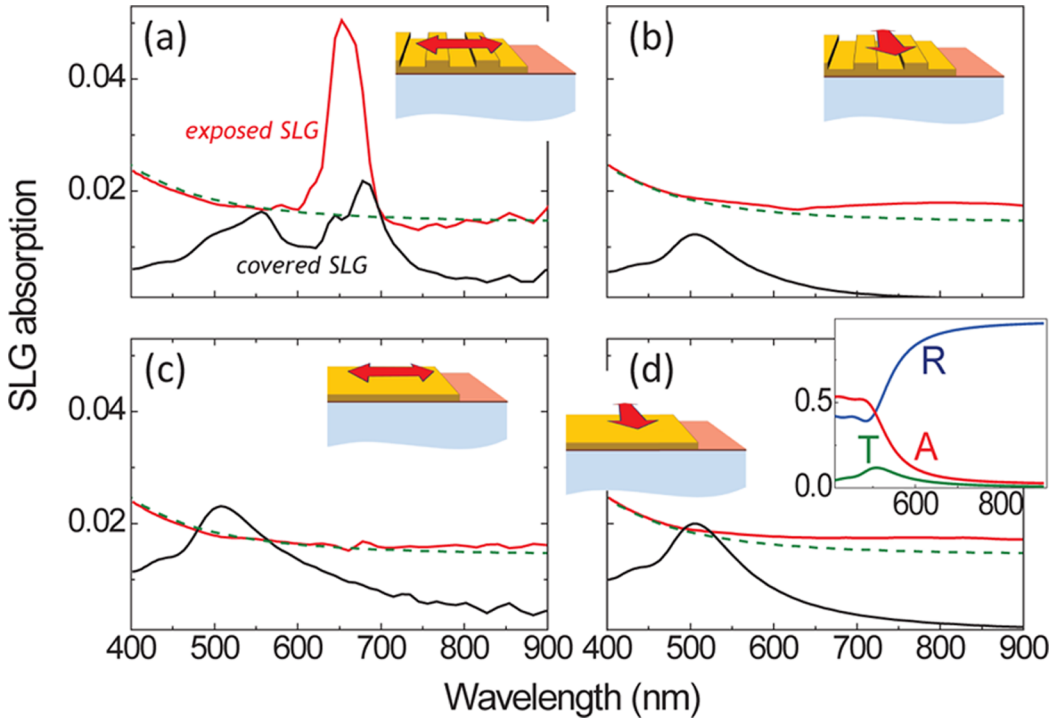

Figure 10. Absorption in the 1 μm exposed part of SLG (red line) and in the covered SLG under the Au contact (black line). The green dotted line is the absorption in 1 μm of SLG on top of SiO_2. All curves are normalized to the light flux incident in 1 μm. (a) TM-polarized and (b) TE-polarized. (c,d) Two polarizations for unpatterned contacts. In cases (b) and (d), a peak at ~500 nm is observed. This is related to a transparency window in Au, as shown in the inset, where the reflection, absorption, and transmission through a 50 nm thick Au film suspended in air are plotted.

where $\epsilon_m(\omega)$ and $\epsilon_d(\omega)$ are the dielectric functions for the metal and dielectric medium, respectively, and the SPP existence condition is $\epsilon_m < -\epsilon_d$.[45,46] k_{SPP} is larger than any propagating wave in the dielectric, whose wavevector is $k = (\omega/c)\sqrt{\epsilon_d}$. This momentum mismatch between SPPs and propagating waves implies that SPPs cannot decay into free propagating waves, but also that one cannot directly excite SPPs from free waves on a smooth metal surface.[45] One way to overcome this is by diffraction, whereby the continuity of the component of momentum parallel to the surface is broken and incident light can scatter into SPPs.[45] This can be achieved by a nanoslit,[59,60] a diffracting element,[61,62] or a grating coupler.[61,63] In the latter case, in particular, a periodic array of metal ridges and grooves delivers the additional momentum according to[45]

$$k_{SPP} = k_{||} \pm mK \tag{2}$$

where $k_{||} = (\omega/c)\sin\theta$ is the parallel component of the incident wavevector, θ the incident angle, $K = 2\pi/a$ the grating's reciprocal lattice vector, a the grating pitch, and m the diffraction order.

We select a grating of 50 nm Au bars periodically placed at a pitch of 620 nm on top of a 50 nm Au contact film, as depicted in Figure 1a, for a 1:1 ratio of ridge and groove widths. These grating parameters are chosen since they were shown to be optimal for yielding a high percentage of incident light scattered into SPPs (~20% in refs 61 and 63). A termination "step" of width d extends beyond the last ridge. For simplicity, we assume the graphene/contact structure to be on top of a semi-infinite SiO_2 substrate. In our simulations, we omit the buried Cr adhesion layer underneath the Au film (used in the experiments), as it does not have a significant impact on the simulation results at the Au–air interface. The dielectric functions of Au[64] and graphene[65] are treated through a Drude–Lorentz model, as explained in ref 44 and in Methods. Inserting Au's dielectric function in eqs 1 and 2, with $\epsilon_d = 1$ for air, yields $\lambda_0 = 645$ nm for the vacuum wavelength of the SPPs at the Au/air interface. It is also possible to have SPPs in the Au/SiO_2 interface. Since $\epsilon_d = 2.13$ for SiO_2,[66] these are excited at $\lambda_0 = 930$ nm. Note that absorption is defined here as the light absorption over a length of graphene, normalized to the light impinging on the same length.

In the first set of calculations, the device is illuminated by a normally incident plane wave polarized perpendicular to the grating (transverse magnetic-TM). This polarization is required because the SPPs are themselves TM waves,[45,46] having both longitudinal (parallel to the propagation direction) and transverse (perpendicular to the surface) electric field components. The exposed part of the single layer graphene (SLG) in-between the contacts is kept fixed at 1000 nm, whereas the width of the Au contact, thus of the SLG unexposed (buried) part, is varied depending on the number of ridges and the size d of the termination step. Periodic and absorbing boundaries are assumed in the lateral and vertical directions, respectively (see Methods). Figure 1b plots the absorption in the exposed SLG normalized to the flux incident on the exposed SLG area, for $d = 0$ and 410 nm. Strong enhancement peaks, reaching up to 5% absorption, are found between 630 and 700 nm. There are also secondary small peaks at ~900–950 nm, assigned to the Au/SiO_2 interface SPPs. The green dashed line indicates the absorption within the 1000 nm wide SLG on top of the semi-infinite SiO_2 substrate in the absence of grating, as derived in the thin film limit [see Methods]

$$A_{SLG} = 4A^0_{SLG}/(n_{SiO_2} + 1)^2 \tag{3}$$

DOI: 10.1021/acs.nanolett.5b02051
Nano Lett. 2016, 16, 8–20

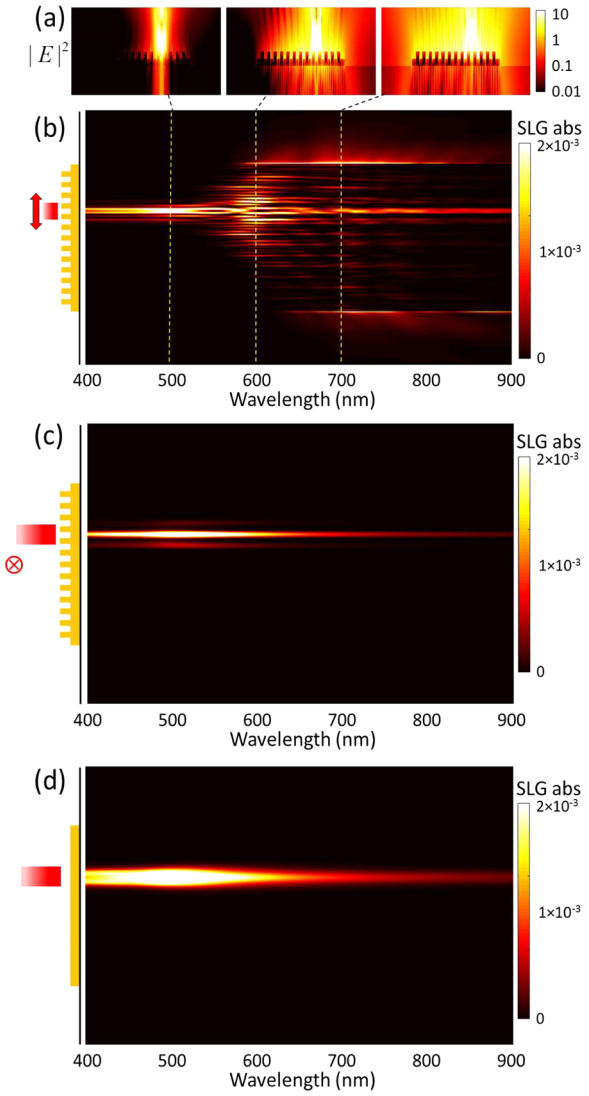

Figure 11. (a) Field intensity distribution for a 1 μm spot illumination at normal incidence (TM), for 500, 600, 700 nm. The color-coding is in logarithmic scale. (b) SLG absorption distribution (vertical axis) as a function of illumination wavelength (horizontal axis). The three wavelengths studied in (a) correspond to three characteristic cases: absorption under the illumination spot, extended absorption under the contact, and absorption in the exposed SLG far from the illumination spot. (c) Same as in (b) but for TE polarization. (d) Same as above for unpatterned contacts (both polarizations yield identical results). Absorptions are normalized to the incident light flux.

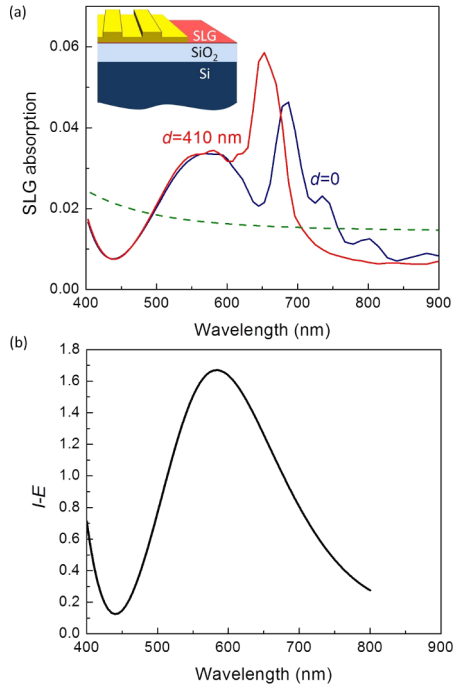

Figure 12. (a) Absorption in the exposed SLG for the system studied in Figure 1 with a SiO_2(300 nm)/Si substrate. (b) Absorption interference enhancement (I–E) without Au contacts. The modulation at ~570 nm is due to I-E.

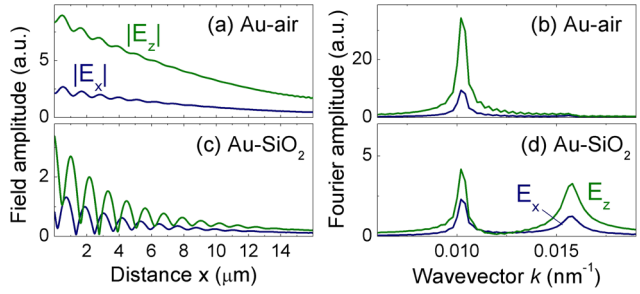

Figure 13. System of Figure 3 in with a SiO_2(300 nm)/Si substrate. Besides a small modulation in the Fourier amplitudes, the SPP characteristics remain the same as for the semi-infinite SiO_2 substrate. Notable is also a deeper "beat" modulation of the field intensity at the Au–SiO_2 interface, due to reflection of the "leaked" SPP at the SiO_2/Si interface.

where $A^0_{SLG} = \pi e^2/\hbar c = 2.3\%$ is the absorption coefficient for suspended SLG in air[27] and $n_{SiO_2} = 1.46$ is the SiO_2 refractive index in the above wavelength range.[66] A 3-fold wavelength-selective increase in absorption is observed, due to coupling with SPPs scattered from the grating.

We now consider the parameter d. Figure 1b indicates that for certain wavelengths (e.g., ~ 630 nm), there are opposite extremes of absorption for the two different steps. Such an asymmetry can be instrumental in designing contact layouts that exhibit a net photovoltage even under uniform illumination. Note that, in the proposed design, photothermal contributions to the photovoltage due to heating of the Au contacts by incident light cancel out, because both contacts absorb the same amount of light. The net photovoltage is purely a result of SPP interference. For the cases pointed out by the two arrows in Figure 1b, we report in Figure 1c the cumulative absorption in the exposed SLG as we move away from the grating edge. In the d = 410 nm case, absorption is strongly enhanced at the edge of the grating and starts leveling off ~300 nm away from it. In contrast, for d = 0 absorption is minimal close to the grating and starts picking up >300 nm from the grating edge. SPP interference causes one contact to "pull" light close to its edge and the other to "push" it away from it. The situation reverses at ~700 nm. To confirm that these light "attraction" and "expulsion" effects are not related to interferences within the contact, i.e., that they are independent of contact width, we perform the same calculations for 9, 11, and 13 ridges. Although we observe some small interference effects at longer wavelengths (>730 nm, especially for d = 0), within the primary wavelength range of interest (630–700 nm) the absorption is independent of grating size. Furthermore, the response is well saturated above 10 grating periods, consistent

DOI: 10.1021/acs.nanolett.5b02051
Nano Lett. 2016, 16, 8–20

with numerical studies on the influence of the number of grating periods.[49−51] To further emphasize that the resulting photoresponse is solely due to SPP interference, we plot in Figure 1d the light absorption in graphene and Au contacts normalized to their thickness and volumetric heat capacity, as well as the differential absorption in graphene and the Au contacts. This shows that the thermal effects in the contacts cancel out in our device design when both contacts are illuminated.

The mechanism responsible for these sharp contrasts in absorption is interference: the excited SPPs travel down the termination step toward the exposed SLG and interfere with the incident waves there, as depicted in Figure 2a. Interference between SPP waves was reported in pure metal systems.[59,60,67,68] To confirm that what shown in Figure 1b is due to interference of SPPs with the incident wave, we examine a series of d values, and plot the absorption in the exposed SLG within the first 100 nm from the contact edge. These calculations are performed at 680 nm, i.e., in-between the two peaks in Figure 1b. An oscillatory response is observed in Figure 2b (points), which is characteristic of interference between two waves with a variable phase between them. The total field at the SLG will be $E_{inc} + E_{SPP}$, where $E_{inc} = 1$ for an incident wave normalized to unit amplitude, and $E_{SPP} = \Delta e^{i(k_{SPP}\cdot d+\phi_0)}$ is the SPP amplitude, with Δ the relative SPP electric field strength compared to the input field, k_{SPP} the SPP wave vector calculated from eq 1 for the Au/air interface, and ϕ_0 a constant phase. We thus fit the SLG absorption of Figure 2b to

$$A = A_{SLG}|1 + \Delta e^{i(k_{SPP}\cdot d+\phi_0)}|^2 \quad (4)$$

where A_{SLG} is evaluated from eq 3. As discussed later, SPPs at the Au/air interface can leak into the dielectric substrate[69] providing an extra loss mechanism. To account for this, we scale the imaginary part of the wave vector $k_{SPP} = Re\{k_{SPP}\}+iIm\{k_{SPP}\}$ according to $Im\{k_{SPP}\} \rightarrow s\cdot Im\{k_{SPP}\}$. We treat Δ, ϕ_0, and s as adjustable parameters and fit eq 4 to the simulation of Figure 2a (note that the oscillation period is dependent only on $Re\{k_{SPP}\}$). An excellent fit is obtained with $\Delta = 1.87$, $\phi_0 = \pi/5$, and $s = 9$, confirming SPP excitation, propagation and interference. The top inset in Figure 2b color codes the absorption within the first 500 nm of exposed SLG as a function of d. The periodic oscillation of light "attraction" and "expulsion" from the contact edge is apparent.

The implication of eq 4 is is that the asymmetry in photovoltage is larger than what seen in Figure 1b. For example, if the two contacts in Figure 1b are placed across each other with a 600 nm gap, then all the light accumulated from both contacts will be funneled close to only one of them. Such a scheme offers great flexibility in designing asymmetric contacts suitable for uniform illumination, eliminating the need for different metallizations.[6] We explore this asymmetric contact design in Figure 2c (see insets). The asymmetric absorption is defined as $A_{asym} = A_R - A_L$, where A_R is the SLG absorption in the 300 nm area close to the right ($d = 0$) contact and A_L is the SLG absorption in the 300 nm area close to the left ($d = 410$ nm) contact. A_{asym} is then proportional to the expected net photovoltage. An antisymmetric response is obtained, as shown in Figure 2c. In particular, at 650 nm (point (i) in Figure 2c), all the flux is "pulled" to the left contact, whereas at 700 nm (point (ii) in Figure 2c), all the flux is "pushed" to the right contact. That is, a spectrally selective region less than 50 nm wide is created, within which the photovoltage abruptly changes sign. Outside this region ($\lambda <$ 580 nm and $\lambda >$ 800 nm), both contacts have similar responses, thus the net photovoltage is zero. Yet, this is not the only response function available. Plotted in Figure 2d is the case of a left contact with $d = 770$ nm. The response is found to be symmetric around 660 nm. In both cases, the peak absorption is 2−3 times higher than what a 600 nm SLG on SiO_2 would absorb in the absence of the contacts. In addition, optimizing the contacts just for the highest absorption (i.e., without creating "clear" symmetric or antisymmetric response functions), the peak absorption exceeds 6%, i.e., a 4-fold increase compared to SLG on SiO_2. If we further limit ourselves to the first 100 nm from the contact edge (i.e., within the junction), then we get an 8-fold enhancement. Further exploration of the system's response, including absorption in the unexposed (buried) SLG under the contact, different light polarizations, unpatterned contacts, and SiO_2 (300 nm)/Si substrate, for both uniform and focused illumination, are consistent with what discussed above (see Methods).

A detailed analysis of all the SPPs that can be launched in our system is performed by considering a patterned contact with a large $d = 20$ μm, illuminated by a narrow 1 μm width TM-polarized source positioned on top of the grating, as shown by the arrow in Figure 3a. In contrast to plane wave incidence, for which $k_{||} = 0$ and where only SPPs compatible with $k_{SPP} = mK$ are excited (see eq 2), the focused beam has $|k_{||}| > 0$ incident wave vector components. It thus allows the full spectrum of SPPs to be excited according to eq 2. Absorbing boundaries are employed in all directions to avoid scattered light from re-entering the computational cell. In Figure 3a, the electric-field intensity distribution is plotted at 650 nm. Strong scattering and fields extending many microns away from the grating are observed, both at the Au/air and Au/SiO_2 interfaces. An intensity oscillation is also observed in the latter, with a period ~1.4 μm. SPPs have both longitudinal and transverse field components, the latter being perpendicular to the metal surface.[45,46] Figure 3b,c plots the longitudinal, $|E_x|$, and transverse, $|E_z|$, electric field amplitudes at the Au/air and Au/SiO_2 interfaces, as a function of distance x from the grating. A simple decay curve is obtained at the top interface, and an oscillating one for the bottom interface. Figure 3d,e report the spatial Fourier transform on these fields. A single peak is found in the top interface, and two in the bottom one: one at exactly the same wavevector as in the top interface, and the other at a larger wavevector. By repeating this procedure at different illumination frequencies we get the SPP dispersion shown in Figure 3f. Lines denote the theoretical dispersion curves from eq 1 using Au's dielectric function and assuming either Au/air or Au/SiO_2 interfaces. Squares indicate the peaks obtained from the simulations by the spatial Fourier transforms. At the Au/air interface, only the Au/air SPP dispersion curve emerges, whereas both Au/air and Au/SiO_2 SPP dispersions are seen at the Au/SiO_2 interface. SPPs are surface waves bound on a metal/dielectric interface because they exist below the light-cone of the dielectric (i.e., the phase-space of free propagating modes defined by $k_{||} \leq n\omega/c$).[45,46] The SPP at the Au/SiO_2 interface is below both the air and SiO_2 light-cones (i.e., $k_{SPP} \geq n_{SiO_2}\omega/c$, $n_{air}\omega/c$) and thus cannot couple to any free radiation states. On the other hand, the SPPs at the Au/air interface are below the air light-cone and within the SiO_2 light-cone (i.e., $n_{air}\omega/c \leq k_{SPP} \leq n_{SiO_2}\omega/c$); thus, they can leak (tunnel) into the

DOI: 10.1021/acs.nanolett.5b02051
Nano Lett. 2016, 16, 8−20

free radiation states of the substrate, explaining why we obtain two SPP signals at the Au/SiO_2 interface. Such leaky waves have been used for SPP characterization within the context of leakage radiation microscopy[69] (a far-field optical method analyzing the leaked SPP waves in glass substrates to characterize SPP propagation on the top interface of a flat or nanostructured metal film[69]). In a semi-infinite substrate, they will just propagate away. In a finite one, on the other hand, part of the leaked waves will be reflected back to the interface and contribute more to the SLG absorption. The dominant effect in photoresponse, however, is the Au/air SPP, as inferred by the Fourier amplitudes in Figures 3b−e, and confirmed by the absorption in Figure 1b, with minimal contribution from Au/SiO_2 SPPs at 930 nm.

Besides photodetection, SPP+incident wave interference in a MGM architecture also lends itself to label-free surface plasmon biosensing,[70−73] whereby SLG assumes the role of an integrated transducer providing direct electrical readout, thus eliminating the need for optical measurements. The use of SLG as an integrated transducer was reported in a dielectric waveguide sensor geometry[74] but not in surface plasmon sensing. Figure 4 assumes that one termination step (sensor arm hereafter) has length d_1 and the other d_2, so that they are at the highest slopes of Figure 2a, i.e., in the midplane of the interference oscillation, with one of them at a positive slope and the other at a negative one. In this setup, the two contacts are in accidental degeneracy, producing the same interference between SPP and incident wave, thus zero net photovoltage under uniform illumination. If now the dielectric environment around the sensor arms changes by the presence of an analyte, this will cause an increase in k_{SPP}, and an additional phase to both SPPs. Having the two arms on a different slope in the response curve of Figure 2a introduces an asymmetry, thus a net photovoltage. The larger the dielectric change, the larger the photovoltage. Also, the longer the sensor arms, the higher the sensitivity, as the SPP will travel a longer distance, therefore sampling more analyte.

Figure 4 numerically tests this idea simulating four pairs of sensor arms, tuned to operate at 678 nm according to Figure 1c: (i) d_1 = 410 nm, d_2 = 750 nm, (ii) d_1 = 775 nm, d_2 = 1075 nm, (iii) d_1 = 1070 nm, d_2 = 1400 nm, and (iv) d_1 = 1435 nm, d_2 = 1730 nm. In cases (i)−(iv), the left arm alternates from being on a positive to a negative slope of the interference diagram of Figure 1c. Thus, the photovoltage in the presence of the analyte is also expected to alternate. For simplicity, the analyte is assumed to be a thin film deposited on the sensor arms and to have n = 1.55, an average value for dry protein films.[75] Figure 4b plots the asymmetric absorption as a function of analyte thickness. We obtain a linear response, with slope increasing the longer the sensor arms. In Figure 4c the absolute value of the slope is plotted as a function of the small sensor arm length d_1, and a good linear fit is obtained. Tuning the arm dimensions thus provides an additional tool for controlling and tuning the device's performance and sensitivity. At long arm lengths, SPP losses will limit the sensitivity, but they could be overcome, e.g., by increasing the metal thickness or reducing the substrate refractive index to limit SPP coupling.

Having demonstrated the design versatility of grating-coupled GPDs, we now show a proof-of-concept experimental validation of our predicted SPP-enhanced SLG absorption and photodetection. The general architecture of our experimental devices with plasmonic grating coupler is shown in Figure 5a, i.e., SLG contacted with metallic source and drain electrodes. In order to quantify the enhancement relative to the no-grating case, we fabricate the grating coupler on top of one of the contacts and leave the other flat. This is the simplest way to break the contacts mirror symmetry and allows the generation of a net non-zero photoresponse, even with both contacts illuminated.

Our devices are fabricated as follows. Graphene is produced by mechanical exfoliation of graphite onto an Si + 300 nm SiO_2[76,77] and characterized by optical microscopy[78] and Raman spectroscopy.[79,80] Subsequently, the source and drain contacts are prepared by e-beam lithography and a base metallization layer is deposited by thermal evaporation of 4 nm Cr and 50 nm Au, employing a lift-off step. The 620 nm period grating is then defined in a further e-beam lithography step by performing a second thermal evaporation of 50 nm Au followed by lift-off. Figure 5b shows a scanning electron micrograph (SEM) of the device. A slight asymmetry between the ridges and grooves is detected due to overexposure during e-beam lithography, but this does not change the spectral characteristics of the grating, solely determined by its period. Afterwards the samples are bonded into a chip carrier for electrical and optical characterization.

We perform wavelength dependent photovoltage mapping to determine the spatial pattern of the devices' photoresponse. Photocurrent mapping is not used due to the fact that a nanovoltmeter is integrated into our setup, allowing maps with higher sensitivity than the available ammeter. We note that photovoltage mapping yields the same results as photocurrent measurements, because photovoltages and photocurrents are proportional to each other. Figure 6 plots the photovoltage maps at different incident wavelengths for polarization perpendicular to the grating (TM-polarization, 100× ultralong working distance objective, numerical aperture NA = 0.6). Figure 6 also shows the structured grating contact and the flat contact without perturbations. At λ = 514 nm the photoresponse occurs predominantly at the edges of the two contacts and is of similar magnitude, but opposite polarity, as expected for a standard MGM PD.[5,7] At 633 nm, Figure 6b indicates that the influence of the grating starts emerging. At 2−3 μm away from the edge of the patterned contact, a photoresponse is detected, even though no junction is present. The effect becomes much more pronounced at 785 nm, where the entire structured contact becomes photosensitive, Figure 6c, and the photoresponse is enhanced ∼400% compared to the flat contact edge. The photoactive area is now determined by the grating area, dominating the photoresponse of the device. When light is impinging on top of the grating where no junction with graphene is present, a strong photoresponse occurs since this light energy is delivered to the junction in graphene at the contact edge, where it is converted into an electrical signal. Furthermore, the responsivity is polarization dependent, as shown in Figure 6d, where the photoresponse is plotted for varying polarization angles of linearly polarized incident 785 nm light. The strongest photoresponse occurs for perpendicular polarization (0°, TM-polarized light). Figure 6e shows the computed asymmetric absorption line-trace assuming a 2 μm wide λ = 700 nm plane source 4 μm above the grating. We plot the absorption in the contact, the exposed graphene and the buried (under the contact) graphene. We find the qualitative features seen in the experiment, i.e., an enlarged active area extending over the patterned contact. Note that, in contrast, in the uniform illumination, these extra contributions cancel out, and a clear interpretation of performance based on

DOI: 10.1021/acs.nanolett.5b02051
Nano Lett. 2016, 16, 8−20

the exposed graphene absorption becomes possible. These experiments are a clear proof-of-concept that the incorporation of a plasmonic grating into the contacts of a graphene-based PD enhances both responsivity and photoactive area.

To have a direct spectral comparison with experiments, we perform calculations with a focused beam illumination (1 μm width) on top of the grating, ~4 μm away from the contact edge, as depicted in Figure 7a. The termination step length is taken as 1250 nm (estimated from the SEM image in Figure 5) and we also include the Si substrate with 300 nm SiO_2. Figure 7b plots the absorption in the exposed SLG, 4 μm away from the illumination spot, for TM and TE polarizations and a flat contact. Both the theoretical spectral and polarization responses are in excellent agreement with experiments and verify the strong responsivity above 700 nm. This contrasts with the normally incident plane wave illumination case, below 700 nm (see Figure 1b). This is understood by considering eq 2 and Figure 3f. For a normally incident plane wave and focused illumination, $k_{\|}$ is zero and non-zero, respectively. Because the latter case is less restrictive for SPP excitation, it gives a wider SPP spectrum at both Au/air and Au/SiO_2 interfaces, thus a wider responsivity compared to the plane wave case (see Methods for details)

In conclusion, we demonstrated the coupling to graphene of surface plasmon polaritons excited in a metallic plasmonic grating and its exploitation in graphene-based photodetection with enhanced responsivity and polarization selectivity. Depending on the grating dimensions, highly tunable spectral selectivity below 50 nm bandwidth can be achieved. Further, the symmetry of the photodetector can be broken, making it active under full illumination, despite identical metal source and drain contacts. The underlying mechanism involves the coupling of light into SPPs on the patterned contact, and their propagation to the exposed SLG area. For uniform coherent illumination, these SPPs can further interfere with the waves directly incident on the exposed SLG, offering a novel tuning capability where the light flux can be attracted or repelled from the contact edge by design. The whole contact thus becomes a highly tunable polarization- and spectral-selective photosensitive area. SPPs and incident wave interference can potentially be exploited for (bio-)sensing by tailoring the grating dimensions. This may allow a novel plasmonic sensing architecture, with high sensitivity and small footprint, with direct electrical readout, without bulky optics.

Methods. *FDTD Simulations.* In our FDTD method, Maxwell's equations are time-integrated on a computational grid

$$\nabla \times \mathbf{E} = -\mu \partial_t \mathbf{H} \tag{5}$$

$$\nabla \times \mathbf{H} = \epsilon_0 \epsilon_\infty \partial_t \mathbf{E} + \partial_t \mathbf{P}_0 + \sum_{j=1}^{N} \partial_t \mathbf{P}_j \tag{6}$$

where material polarization is taken into account through polarizabilities $\mathbf{P}$

$$\partial_t^2 \mathbf{P}_0 + \gamma \partial_t \mathbf{P}_0 = \omega_p^2 \epsilon_0 \mathbf{E} \tag{7}$$

$$\partial_t^2 \mathbf{P}_j + \Gamma_j \partial_t \mathbf{P}_j + \Omega_j^2 \mathbf{P}_j = \Delta\epsilon_j \Omega_j^2 \epsilon_0 \mathbf{E} \tag{8}$$

At a point in a dispersive material, each relevant polarizability term contributes to an absorption

$$A_j = (1/2)\mathrm{Re}(\mathbf{J}_j^* \cdot \mathbf{E}) \tag{9}$$

where the polarization current is $\mathbf{J}_j = \partial_t \mathbf{P}_j$. Upon Fourier transforming the time series of $\mathbf{E}$ and $\mathbf{J}_j$ we obtain the spectral absorption at every point in graphene. The polarization equations imply a Drude–Lorentz model for the dielectric function[81]

$$\epsilon(\omega) = \epsilon_\infty - \frac{\omega_p^2}{\omega^2 + i\omega\gamma} + \sum_{j=1}^{N} \frac{\Delta\epsilon_j \Omega_j^2}{\Omega_j^2 - \omega^2 - i\omega\Gamma_j} \tag{10}$$

where the first term is the Drude free-electron contribution and the second contains Lorentz oscillators corresponding to interband transitions. ω_p and $1/\gamma$ are the free electron plasma frequency and relaxation time, Ω_j, $\Delta\epsilon_j$, Γ_j are transition frequency, oscillator strength, and decay rate for the Lorentz terms. To accurately reproduce the experimental dielectric functions (Au from ref 64 and Si from ref 66), we treat these as fit parameters. For Au we use $N = 4$, and $\epsilon_\infty = 4.054$, $\Delta\epsilon_j = (0.43, 0.634, 0.755, 1.059)$, $\hbar\omega_p = 8.76$ eV, $\hbar\gamma = 0.068$ eV, $\hbar\Omega_j = (2.67, 3.03, 3.54, 4.23)$eV, and $\hbar\Gamma_j = (0.458, 0.641, 0.892, 0.959)$eV. For Si, we use $N = 7$ without any Drude term: $\epsilon_\infty = 1.89$, $\Delta\epsilon_j = (1.198, 0.963, 1.021, 1.164, 1.407, 2.259, 1.869)$, $\hbar\Omega_j = (3.39, 3.51, 3.68, 3.86, 4.06, 4.25, 4.61)$eV, and $\hbar\Gamma_j = (0.188, 0.203, 0.239, 0.269, 0.283, 0.265, 0.0)$eV. Figure 8 plots our model dielectric functions along with the experimental ones, showing an excellent agreement.

The computational cell comprises a 2 nm cubic grid. Perfectly matched layer (PML) boundary conditions[82] are applied at the edges of the cell in the vertical direction. In the lateral direction, we use periodic boundary conditions for the uniform illumination case, and PML for the focused. We use a broadband source to get the entire spectrum with a single simulation, and upon Fourier transform, we get the corresponding spectral response.

SLG Index of Refraction. The index of refraction of SLG was measured by ellipsometry for wavelengths up to 750 nm in ref 65. To extrapolate to longer wavelengths, we assume undoped SLG and use the universal optical conductance $\sigma = e^2/4\hbar$, to get the dielectric function

$$\epsilon = \epsilon_\infty + i\frac{4\pi\sigma}{\omega d_{\mathrm{SLG}}} = \epsilon_\infty + i\frac{\alpha\lambda}{2d_{\mathrm{SLG}}} \tag{11}$$

where $d_{\mathrm{SLG}} = 0.335$ nm is the SLG's thickness and $\alpha = e^2/\hbar c$ is the fine structure constant. In the thin film limit, eq 11 yields

$$A_{\mathrm{SLG}}^0 \cong \mathrm{Im}(\epsilon)\frac{2\pi d_{\mathrm{SLG}}}{\lambda} = \pi\alpha = 2.3\% \tag{12}$$

A value of $\epsilon_\infty = 5.7$ ensures that eq 11 matches the ellipsometric experimental data of ref 65 at smaller wavelengths. We fit a Drude–Lorentz model to both the ellipsometric data at small wavelengths and eq 11 at longer wavelengths, Figure 9a. In Figure 9b the resulting SLG absorption is plotted. The Drude–Lorentz model for SLG uses $N = 4$ with $\epsilon_\infty = 2.148$, $\Delta\epsilon_j = (64.8, 2.92, 1.69)$, $\hbar\omega_p = 1.34$ eV, $\hbar\gamma = 0.7$ eV, $\hbar\Omega_j = (1.0, 4.0, 4.56)$ eV, and $\hbar\Gamma_j = (5.41, 2.77, 1.0)$ eV. Within FDTD's 2 nm grid, SLG is treated as an effective 2 nm thick slab. Its dielectric function is scaled to reproduce the correct absorption and reflection properties according to $\epsilon \to 1 + (\epsilon - 1)d_{\mathrm{SLG}}/2$, i.e., $\epsilon_\infty \to 1.192$ and $\Delta\epsilon_j \to (10.85, 0.488, 0.283)$.

Approximating graphene by a thin effective slab has been a well-established practice for full electromagnetic simulations,[83,84] where good convergence is found even for effective thicknesses of up to several nms.[85,86]

DOI: 10.1021/acs.nanolett.5b02051
Nano Lett. 2016, 16, 8–20

SLG Absorption in the Thin Film Limit. In a three-layer system, the normal incidence Fresnel equations for reflection and transmission amplitudes are[87,88]

$$r = r_{12} + \frac{t_{12}r_{23}t_{21}e^{2i\phi}}{1 - r_{12}r_{23}e^{2i\phi}} \tag{13}$$

$$t = \frac{t_{12}t_{23}e^{i\phi}}{1 - r_{12}r_{23}e^{2i\phi}} \tag{14}$$

where $r_{ij} = (n_i - n_j)/(n_i + n_j)$, $t_{ij} = 2n_i/(n_i + n_j)$, and $\phi = n_2\omega d_2/c$, with d_2 the film thickness. Here, we assume the incoming medium $n_1 \equiv n_{air} = 1$, the film $n_2 \equiv n_{SLG}$ and the semi-infinite substrate $n_3 \equiv n_{SiO_2}$. Reflection and transmission coefficients are $R = |r|^2$ and $T = n_3|t|^2$. In the thin film limit, using the SLG dielectric function given by eq 11, we get

$$R \cong \left(\frac{n_1 - n_2}{n_1 + n_3}\right)^2\left(1 - \frac{4\beta n_1}{n_1^2 - n_3^2} + \left|\frac{\beta(\varepsilon - n_1n_3)}{Im\{\varepsilon\}(n_3 - n_1)}\right|^2\right) \tag{15}$$

$$T \cong \frac{4n_1n_3}{(n_1 + n_3)^2}\left(1 - \frac{2\beta}{n_1 + n_3}\right) \tag{16}$$

where $\beta = 2\pi d Im\{\epsilon\}/\lambda = N\pi\alpha$, ϵ is the film dielectric constant, $\alpha = e^2/\hbar c$ is the fine structure constant, and $d = Nd_{SLG}$ is the N-layer graphene (NLG) thickness. This results in an absorption

$$A = 1 - R - T \cong N\pi\alpha\frac{4n_1}{(n_1 + n_3)^2} \tag{17}$$

whereas for a NLG suspended in a uniform medium (i.e., $n_1 = n_3 = n$), we find $A = N\pi\alpha/n = 2.3/n\%$. These equations are valid for $N < 10$.[27,78,89] For $N > 10$, the thin film limit breaks down and the optical paths inside the film must be taken into account.

Regarding reflection, this is typically dominated by the substrate since the difference in refractive index is usually largest between air and the substrate. However, in the $n_1 = n_3 = n$ case the third term in the right-hand side of eq 15 is the only non-zero term, resulting in NLG reflection: $R \cong N^2\pi^2d_{SLG}^2|\epsilon - n^2|^2/(n^2\lambda^2)$. This is very small for SLG ($R \cong 0.02\%$ at 600 nm for suspended SLG[27]), but it increases quadratically with N.

Coherent Uniform Illumination. Figure 10 plots the response of our system considering the absorption in both exposed and covered SLG for both polarizations and patterned and unpatterned contacts. For simplicity, we only consider the $d = 410$ nm case with 13 ridge periods. We find that, in all cases other than TM-excitation on the patterned contact, the absorption in the exposed SLG is similar to that of a SLG on top of SiO_2 in the absence of the contact (green dotted line). Interestingly, there is some absorption in the covered SLG as well. In the TM-excitation of the patterned contact, we obtain a similar modulation with wavelength as that in the exposed SLG, albeit of significantly smaller magnitude. We note that, in order to directly compare with the exposed SLG absorption, we still normalize to the power illuminating the exposed SLG area. Had we normalized to the flux illuminating the whole contact, then the covered SLG absorption would appear with a much smaller magnitude than in Figure 10. We also obtain absorption in the other cases as well, peaked at ~500 nm. This, however, is irrelevant to the grating and SPPs, as it is there that Au becomes most transparent. Au is strongly absorptive at high energies because of the onset of interband transitions from its d-electrons,[64] whereas it is strongly reflective at small energies because of its conduction electrons.[64] The inset in Figure 10d plots the reflection, transmission, and absorption coefficients through a 50 nm thick Au film in air, displaying Au's transparency window at ~500 nm.

Focused illumination. We now explore the case of focused illumination on the grating, which more closely resembles the experiments. To better facilitate the simulation and avoid having laterally scattered light re-enter the computational cell, we remove the lateral periodic boundary conditions and adopt PML boundary conditions,[82] so that any light scattered toward the sides of the computational cell permanently exits the calculations. We also consider a much larger exposed SLG area for better visualization. We adopt a TM polarized 1 μm-wide plane source illuminating the 13-period $d = 410$ nm grating at a non-symmetric position, as depicted in Figure 11. The frequency domain electric-field intensity profiles for $\lambda = 500$, 600, and 700 nm are shown in logarithmic scale in Figure 11a. No scattering occurs at 500 nm, whereas the most intense is seen at 700 nm.

The system's full response is shown in Figure 11b, where we plot the SLG absorption throughout the length of the structure (vertical axis) for different wavelengths (horizontal axis). The illumination source is again a TM-polarized 1 μm wide spot, as shown in the inset schematic. Absorption is normalized to the peak incoming flux per unit area. Three distinct regions emerge: up to 550 nm, absorption only occurs in the covered SLG directly underneath the illumination source. For 550 nm < λ < 650 nm, increased absorption is found in an extended area (several microns away from the illumination spot) in the covered SLG, pointing toward light diffraction into SPPs at the Au−SiO_2 interface. Above 650 nm there is strong absorption in the exposed SLG beyond the grating. This points toward light diffraction into SPPs in the Au−air interface, which propagate and reach exposed SLG at the grating's edge. In Figure 11c, we plot the same absorption map for TE illumination of a patterned contact, whereas in Figure 11d for illumination of an unpatterned contact. In both cases, no absorption is found, except directly underneath the illumination spot. It is thus clear that SPP-mediated effects dominate the response for TM-polarized illumination.

SiO_2/Si Substrate Effects. The SiO_2 (300 nm)/Si substrate has two effects. First, it provides some interference-based enhancement of the SLG absorption.[90−93] Figure 12a plots the exposed SLG absorption for the system described in Figure 1 on top of a 300 nm SiO_2/Si substrate. The response is similar to the semi-infinite SiO_2 case, except for an overall modulation due to the interference effects in the SiO_2 dielectric spacer. The net interference-enhancement (I-E) effect on absorption (i.e., without the patterned contact) is plotted in Figure 12b. The dielectric spacer can thus give additional degrees of freedom (i.e., the spacer's index and thickness) in optimizing the system's response. We also simulated the asymmetric contact layouts studied in Figure 1d on 300 nm SiO_2/Si and found that they produce a very similar response, irrespective of the finite dielectric spacer. This is expected, since I-E partially cancels out when considering asymmetric absorption. The second effect of the 300 nm SiO_2/Si substrate is that the leaked SPPs at the Au−air interface will be reflected back from the Si substrate. Figure 13 plots the field intensities along the two Au interfaces, as well as the corresponding Fourier transform amplitudes (see Figure 3b−e for the 300 nm SiO_2/Si case). We note a deeper

DOI: 10.1021/acs.nanolett.5b02051
Nano Lett. 2016, 16, 8−20

"beat" modulation on the Au−SiO_2 interface, due to the back reflected fields of the "leaked" Au−air SPP. This is also apparent in the Fourier amplitude. However, no frequency shifts are observed in the latter. We thus conclude that, other than some small amplitude modulations, the SPP structure is largely unaffected by the SiO_2 being 300 nm thick or semi-infinite.

AUTHOR INFORMATION

Corresponding Author

*E-mail: acf26@cam.ac.uk.

Notes

The authors declare no competing financial interest.

ACKNOWLEDGMENTS

We acknowledge funding from EU Graphene Flagship (no. 604391), ERC Grant Hetero2d, EPSRC Grants EP/K01711X/1, EP/K017144/1, EU grant GENIUS, a Royal Society Wolfson Research Merit Award.

REFERENCES

(1) Ferrari, A. C.; et al. *Nanoscale* **2015**, *7*, 4598.
(2) Koppens, F. H. L.; Mueller, T.; Avouris, Ph.; Ferrari, A. C.; Vitiello, M. S.; Polini, M. *Nat. Nanotechnol.* **2014**, *9*, 780−793.
(3) Urich, A.; Unterrainer, K.; Mueller, T. *Nano Lett.* **2011**, *11*, 2804.
(4) Xia, F. N.; Mueller, T.; Lin, Y. M.; Valdes-Garcia, A.; Avouris, Ph. *Nat. Nanotechnol.* **2009**, *4*, 839.
(5) Lee, E. J. H.; Balasubramanian, K.; Weitz, R. T.; Burghard, M.; Kern, K. *Nat. Nanotechnol.* **2008**, *3*, 486.
(6) Mueller, T.; Xia, F.; Avouris, Ph. *Nat. Photonics* **2010**, *4*, 297.
(7) Mueller, T.; Xia, F.; Freitag, M.; Tsang, J.; Avouris, Ph. *Phys. Rev. B: Condens. Matter Mater. Phys.* **2009**, *79*, 245430.
(8) Lemme, M. C.; Koppens, F. H. L.; Falk, A. L.; Rudner, M. S.; Park, H.; Levitov, L. S.; Marcus, C. M. *Nano Lett.* **2011**, *11*, 4134.
(9) Echtermeyer, T. J.; Britnell, L.; Jasnos, P. K.; Lombardo, A.; Gorbachev, R. V.; Grigorenko, A. N.; Geim, A. K.; Ferrari, A. C.; Novoselov, K. S. *Nat. Commun.* **2011**, *2*, 458.
(10) Liu, Y.; Cheng, R.; Liao, L.; Zhou, H.; Bai, J.; Liu, G.; Liu, L.; Huang, Y.; Duan, X. *Nat. Commun.* **2011**, *2*, 579.
(11) Gabor, N. M.; Song, J. C. W.; Ma, Q.; Nair, N. L.; Taychatanapat, T.; Watanabe, K.; Taniguchi, T.; Levitov, L. S.; Jarillo-Herrero, P. *Science* **2011**, *4*, 648.
(12) Konstantatos, G.; Badioli, M.; Gaudreau, L.; Osmond, J.; Bernechea, M.; Garcia de Arquer, P.; Gatti, F.; Koppens, F. H. L. *Nat. Nanotechnol.* **2012**, *7*, 363.
(13) Engel, M.; Steiner, M.; Lombardo, A.; Ferrari, A. C.; Loehneysen, H. V.; Avouris, Ph.; Krupke, R. *Nat. Commun.* **2012**, *3*, 906.
(14) Yan, J.; Kim, M.-H.; Elle, J. A.; Sushkov, A. B.; Jenkins, G. S.; Milchberg, H. M.; Fuhrer, M. S.; Drew, H. D. *Nat. Nanotechnol.* **2012**, *7*, 472.
(15) Chitara, B.; Krupanidhi, S. B.; Rao, C. N. R. *Appl. Phys. Lett.* **2011**, *99*, 113114.
(16) Freitag, M.; Low, T.; Zhu, W.; Yan, H.; Xia, F.; Avouris, Ph. *Nat. Commun.* **2013**, *4*, 1951.
(17) Vicarelli, L.; Vitiello, M. S.; Coquillat, D.; Lombardo, A.; Ferrari, A. C.; Knap, W.; Polini, M.; Pellegrini, V.; Tredicucci, A. *Nat. Mater.* **2012**, *11*, 865.
(18) Spirito, D.; et al. *Appl. Phys. Lett.* **2014**, *104*, 061111.
(19) Cai, X.; et al. *Nat. Nanotechnol.* **2014**, *9*, 814−819.
(20) Park, J.; Ahn, Y. H.; Ruiz-Vargas, C. *Nano Lett.* **2009**, *9*, 1742.
(21) Song, J. C. W.; Rudner, M. S.; Marcus, C. M.; Levitov, L. S. *Nano Lett.* **2011**, *11*, 4688.
(22) Echtermeyer, T. J.; et al. *Nano Lett.* **2014**, *14*, 3733.
(23) Giovannetti, G.; Khomyakov, P. A.; Brocks, G.; Karpan, V. M.; van den Brink, J.; Kelly, P. J. *Phys. Rev. Lett.* **2008**, *101*, 026803.
(24) Peters, E. C.; Lee, E. J. H.; Burghard, M.; Kern, K. *Appl. Phys. Lett.* **2010**, *97*, 193102.
(25) Rao, G.; Freitag, M.; Chiu, H.-Y.; Sundaram, R. S.; Avouris, Ph. *ACS Nano* **2011**, *5*, 5848.
(26) Sun, D.; et al. *Nat. Nanotechnol.* **2012**, *7*, 114.
(27) Nair, R. R.; Blake, P.; Grigorenko, A. N.; Novoselov, K. S.; Booth, T. J.; Stauber, T.; Peres, N. M. R.; Geim, A. K. *Science* **2008**, *320*, 1308.
(28) Mak, K. F.; Sfeir, M. Y; Wu, Y; Lui, C. H.; Misewich, J. A.; Heinz, T. F. *Phys. Rev. Lett.* **2008**, *101*, 196405.
(29) Lagatsky, A. A.; et al. *Appl. Phys. Lett.* **2013**, *102*, 013113.
(30) Sze, S. M. *Physics of Semiconductor Devices*; Wiley Interscience: New York, 1981.
(31) Kim, C. O.; Kim, S.; Shi, D. H.; Kang, S. S.; Kim, J. M.; Jang, C. W.; Joo, S. S.; Lee, J. S; Kim, J. H.; Choi, S.-H.; Hwang, E. *Nature Commun.* **2014**, *5*, 3249.
(32) Britnell, L.; et al. *Science* **2013**, *340*, 1311.
(33) Roy, K.; Padmanabhan, M.; Goswami, S.; Sai, T. P.; Ramalingam, G.; Raghavan, S.; Ghosh, A. *Nat. Nanotechnol.* **2013**, *8*, 826−830.
(34) An, X.; Liu, F.; Jung, Y. J.; Kar, S. *Nano Lett.* **2013**, *13*, 909.
(35) Liu, F.; Kar, S. *ACS Nano* **2014**, *8*, 10270.
(36) Schall, D.; et al. *ACS Photonics* **2014**, *1*, 781.
(37) Furchi, M.; et al. *Nano Lett.* **2012**, *12*, 2773−2777.
(38) Engel, M.; et al. *Nat. Commun.* **2012**, *3*, 906.
(39) Shiue, R.; Gan, X.; Gao, Y.; Li, L.; Yao, X.; et al. *Appl. Phys. Lett.* **2013**, *105*, 241109.
(40) Pospischil, A.; et al. *Nat. Photonics* **2013**, *7*, 892−896.
(41) Gan, X.; et al. *Nat. Photonics* **2013**, *7*, 883−887.
(42) Wang, X.; Cheng, Z.; Xu, K.; Tsang, H. K.; Xu, J. *Nat. Photonics* **2013**, *7*, 888−891.
(43) Fang, Z.; Liu, Z.; Wang, Y.; Ajayan, P. M.; Nordlander, P.; Halas, N. J. *Nano Lett.* **2012**, *12*, 3808.
(44) Schedin, F.; Lidorikis, E.; Lombardo, A.; Kravets, V. G.; Geim, A. K.; Grigorenko, A. N.; Novoselov, K. S.; Ferrari, A. C. *ACS Nano* **2010**, *4*, 5617.
(45) Maier, S. A. *Plasmonics: Fundamentals and Applications*; Springer-Verlag: Berlin, 2007.
(46) Raether, H. *Surface Plasmons*; Springer-Verlag: Berlin, 1988.
(47) Economou, E. N. *Phys. Rev.* **1969**, *182*, 539.
(48) Ishi, T.; Fujikata, J.; Makita, K.; Baba, T.; Ohashi, K. *Jpn. J. Appl. Phys.* **2005**, *44*, 364.
(49) Ren, F.-F.; Ang, K.-W.; Ye, J.; Yu, M.; Lo, G.-Q.; Kwong, D.-L. *Nano Lett.* **2011**, *11*, 1289.
(50) Yu, Z.; Veronis, G.; Fan, S.; Brongersma, M. L. *Appl. Phys. Lett.* **2006**, *89*, 151116.
(51) Bhat, R. D.; Panoiu, N. C.; Brueck, S. R.; Osgood, R. M. *Opt. Express* **2008**, *16*, 4588.
(52) Shackleford, J. A.; Grote, R.; Currie, M.; Spanier, J. E.; Nabet, B. *Appl. Phys. Lett.* **2009**, *94*, 083501.
(53) Karar, A.; Das, N.; Tan, C. L.; Alameh, K.; Lee, Y. T.; Karouta, F. *Appl. Phys. Lett.* **2011**, *99*, 133112.
(54) Tielrooij, K. J.; Piatkowski, L.; Massicotte, M.; Woessner, A.; Ma, Q.; Lee, Y.; Myhro, K. S.; Lau, C. N.; Jarillo-Herrero, P.; van Hulst, N. F.; Koppens, F. H. L. *Nat. Nanotechnol.* **2015**, *10*, 437.
(55) Tielrooij, K. J.; Massicotte, M.; Piatkowski, L.; Woessner, A.; Ma, Q.; Jarillo-Herrero, P.; van Hulst, N. F.; Koppens, F. H. L. *J. Phys.: Condens. Matter* **2015**, *27*, 164207.
(56) Harrer, A.; Schwarz, B.; Gansch, R.; Reininger, P.; Detz, H.; Zederbauer, T.; Andrews, A. M.; Schrenk, W.; Strasser, G. *Appl. Phys. Lett.* **2014**, *105*, 171112.
(57) Wang, Z.; Ishibashi, K.; Komiyama, S.; Nagai, N.; Hirakawa, K. *Appl. Phys. Lett.* **2012**, *101*, 091114.
(58) Taflove, A.; Hagness, S. C. *Computational electrodynamics: the finite difference time-domain method*; Artech House: Boston, MA, 2005.
(59) López-Tejeira, F.; et al. *Nat. Phys.* **2007**, *3*, 324.
(60) Choi, S. B.; et al. *Appl. Phys. Lett.* **2009**, *94*, 063115.

DOI: 10.1021/acs.nanolett.5b02051
Nano Lett. 2016, 16, 8−20

(61) Radko, I. P.; Bozhevolnyi, S. I.; Brucoli, G.; Martín-Moreno, L.; García-Vidal, F. J.; Boltasseva, A. *Phys. Rev. B: Condens. Matter Mater. Phys.* **2008**, *78*, 115115.
(62) Søndergaard, T.; Siahpoush, V.; Jung, J. *Phys. Rev. B: Condens. Matter Mater. Phys.* **2012**, *86*, 085455.
(63) Lévêque, G.; Martin, O. J. F. *J. Appl. Phys.* **2006**, *100*, 124301.
(64) Johnson, P. B.; Christy, R. W. *Phys. Rev. B* **1972**, *6*, 4370.
(65) Kravets, V. G.; Grigorenko, A. N.; Nair, R. R.; Blake, P.; Anissimova, S.; Novoselov, K. S.; Geim, A. K. *Phys. Rev. B: Condens. Matter Mater. Phys.* **2010**, *81*, 155413.
(66) Palik, E. D. *Handbook of Optical Constants of Solids*; Academic: San Diego, CA, 1998.
(67) Weeber, J.-C.; Bouhelier, A.; Colas des Francs, G.; Markey, L.; Dereux, A. *Nano Lett.* **2007**, *7*, 1352.
(68) Zia, R.; Brongersma, M. L. *Nat. Nanotechnol.* **2007**, *2*, 426.
(69) Drezet, A.; et al. *Mater. Sci. Eng., B* **2008**, *149*, 220.
(70) Brolo, A. G. *Nat. Photonics* **2012**, *6*, 709.
(71) Homola. *Chem. Rev.* **2008**, *108*, 462−493.
(72) Gao, Y.; Gan, Q.; Xin, Z.; Cheng, X.; Bartoli, F. J. *ACS Nano* **2011**, *5*, 9836−9844.
(73) Feng, J.; Siu, V. S.; Roelke, A.; Mehta, V.; Rhieu, S. Y.; Palmore, G. T. R.; Pacifici, D. *Nano Lett.* **2012**, *12*, 602−609.
(74) Kim, J.; Kasture, M.; Hwang, T.; Kulkarni, A.; Amin, R.; Park, S.; Kim, T.; Gosavi, S. *Appl. Biochem. Biotechnol.* **2012**, *167*, 1069−1075.
(75) Voros, J. *Biophys. J.* **2004**, *87*, 553.
(76) Novoselov, K. S.; Geim, A. K.; Morozov, S. V.; Jiang, D.; Zhang, Y.; Dubonos, S. V.; Grigorieva, I. V.; Firsov, A. A. *Science* **2004**, *306*, 666.
(77) Novoselov, K. S.; Jiang, D.; Schedin, F.; Booth, T. J.; Khotkevich, V.; Morozov, S. V.; Geim, A. K. P. *Proc. Natl. Acad. Sci. U. S. A.* **2005**, *102*, 10451.
(78) Casiraghi, C.; et al. *Nano Lett.* **2007**, *7*, 2711.
(79) Ferrari, A. C.; Meyer, J. C.; Scardaci, V.; Casiraghi, C.; Lazzeri, M; Mauri, F.; Piscanec, S.; Jiang, D.; Novoselov, K. S.; Roth, S.; Geim, A. K. *Phys. Rev. Lett.* **2006**, *97*, 187401.
(80) Ferrari, A. C.; Basko, D. M. *Nat. Nanotechnol.* **2013**, *8*, 235.
(81) Wooten, F. *Optical Properties of Solids*; Academic Press: New York, 1972.
(82) Chen, J. C.; Li, K. *Microw. Opt. Techn. Lett.* **1995**, *10*, 319.
(83) Vakil, A.; Engheta, N. *Science* **2011**, *332*, 1291.
(84) Koppens, F. H. J.; Chang, D. E.; García de Abajo, F. J. *Nano Lett.* **2011**, *11*, 3370.
(85) Ding, K.; Shen, Y.; Ng, J.; Zhou, L. *EPL* **2013**, *102*, 28005.
(86) Cheng, J.; Wang, W. L.; Mosallaei, H.; Kaxiras, E. *Nano Lett.* **2014**, *14*, 50.
(87) Anders, H. *Thin Films in Optics*; Focal: London, 1967.
(88) Hecht, E. *Optics*, 4th ed.; Addison Wesley: Boston, MA, 2002.
(89) Kuzmenko, A. B.; van Heumen, E.; Carbone, F.; van der Marel, D. *Phys. Rev. Lett.* **2008**, *100*, 117401.
(90) Wang, Y. Y.; Ni, Z. H.; Shen, Z. X.; Wang, H. M.; Wu, Y. H. *Appl. Phys. Lett.* **2008**, *92*, 043121.
(91) Yoon, D.; Moon, H.; Son, Y.-W.; Choi, J. S.; Park, B. H.; Cha, Y. H.; Kim, Y. D.; Cheong, H. *Phys. Rev. B: Condens. Matter Mater. Phys.* **2009**, *80*, 125422.
(92) Gao, L.; Ren, W.; Liu, B.; Saito, R.; Wu, Z.-S.; Li, S.; Jiang, C.; Li, F.; Cheng, H.-M. *ACS Nano* **2009**, *3*, 933.
(93) Klar, P.; Lidorikis, E.; Eckmann, A.; Verzhbitskiy, I. A.; Ferrari, A. C.; Casiraghi, C. *Phys. Rev. B: Condens. Matter Mater. Phys.* **2013**, *87*, 205435.

DOI: 10.1021/acs.nanolett.5b02051
Nano Lett. 2016, 16, 8−20